Impact of processing gas composition on process stability and properties of PBF-LB/M processed alloy 718

Citation for the original published paper (version of record):
Deckers, T., Jabir Hussain, A., Kersting, L. et al (2024). Impact of processing gas composition on process stability and properties of PBF-LB/M processed alloy 718. Journal of Manufacturing Processes, 120: 712-718.
http://dx.doi.org/10.1016/j.jmapro.2024.04.061

Journal of Manufacturing Processes 120 (2024) 712–718

Contents lists available at ScienceDirect

Journal of Manufacturing Processes

journal homepage: www.elsevier.com/locate/manpro

Impact of processing gas composition on process stability and properties of PBF-LB/M processed alloy 718

T. Deckers [a,d,*], A. Fardan [b,*], L. Kersting [c], A. Kreutzer [c], P. Forêt [a], S. Dubiez-Le Goff [a], G. Witt [d], S. Kleszczynski [d], U. Klement [b], E. Hryha [b]

[a] Linde GmbH, 85716 Unterschleißheim, Germany
[b] Department of Industrial and Materials Science, Chalmers University of Technology, 412 96 Göteborg, Sweden
[c] Siemens Energy AG, 10553 Berlin, Germany
[d] University Duisburg-Essen, Department of Manufacturing Technologies, 47057 Duisburg, Germany

ARTICLE INFO

Keywords:
PBF-LB/M
Process gas
Alloy 718
EBSD
Optical tomography
Helium
Hydrogen

ABSTRACT

The almost unlimited design freedom of the laser-based powder bed fusion of metals (PBF-LB/M) makes this technology very attractive for industry. However, as a developing technology, it still faces some challenges when it comes to productivity and robustness, to name some. Whereas numerous studies covered the impact of laser-based parameters on material properties and robustness, the effect of the processing gas received limited attention. The objective of this study was to evaluate the effect of processing gas composition, containing helium (He) and hydrogen (H_2), compared to conventionally used argon (Ar), during PBF-LB/M processing of virgin alloy 718 powder, on printing behavior and part properties. The four gases studied were Ar, Ar +30%He, Ar +30%He +2%H_2, and Ar +70%He. Optical Tomography (OT) was used to monitor process stability, which unveiled a significant decrease in process-by products (spatters) between 51 % and 89 % using He and H_2-containing gases. It was also found that the process gas decreased the bulk porosity from an average value of 0.08 % when processed with Ar to 0.04 % when using Ar + 70%He. The oxygen pickup by the spatter particles was reduced from 630 ppm (Ar) to 331 ppm (Ar +70%He). EBSD analysis revealed that there were no evident changes in microstructure with the processing gas. The samples processed also had similar tensile properties with yield and ultimate tensile strength of 1180 MPa and 1395 MPa, respectively. However, there was a slight increase in ductility from 16.5 % to 17.2 %, when processed with pure Ar and Ar + 70%He, respectively. This study shows that utilizing standard Ar processing atmosphere with He addition leads to a more stable process with reduced spatter, porosity and a marginal increase in ductility for Alloy 718.

1. Introduction

Laser-based powder bed fusion of metals (PBF-LB/M) is considered one of the most widespread manufacturing technologies within additive manufacturing (AM) [1]. A part is created layer-by-layer with a laser by melting and consolidating metal powder without molds or tools. Thus, geometries of almost any complexity can be built, which is different from most manufacturing processes [2]. Until now, the processing of selected alloys has been optimized primarily through extensive process parameter optimization [3]. Thus, new parameter sets were defined, focusing on geometric accuracy or productivity rather than on a combination of both. Recent studies addressed the process atmosphere as a relevant and adjustable parameter [4–7]. This offers additional benefits beyond solely configuring the laser parameters. Various studies have identified the influences of novel process gases that deviate from argon and nitrogen. Pauzon et al. [6] increased the productivity of Ti-6Al-4 V by adding He to the process gas. In addition to reducing printing time, Deckers et al. [4] observed a reduction in the surface roughness of alloy 718 samples. H_2 and He differ from conventionally used nitrogen and argon in several aspects. Both novel PBF-LB/M process gases exhibit a much lower density, which enables higher flow speeds [8]. Bidare et al. [5] investigated the correlation between process gases and chamber pressures to influence the melt pool geometries. Furthermore, the different thermal conductivity and heat capacity of novel gas mixtures in contrast to argon and nitrogen can affect the microstructure based on part design and selected process parameters [8–10].

* Corresponding authors.
E-mail addresses: tobias.deckers@linde.com (T. Deckers), fardan@chalmers.se (A. Fardan).

https://doi.org/10.1016/j.jmapro.2024.04.061
Received 18 July 2023; Received in revised form 22 April 2024; Accepted 23 April 2024
Available online 3 May 2024

Nickel-based superalloys are used due to their superior corrosion and high-temperature resistance up to 1000 °C [11]. Applications range from power, chemical, and petrochemical industries to aerospace. Typical components from these superalloys can be found in, e.g., jet engines and gas turbines [11,12]. One of these superalloys is commonly known as alloy 718. It is well established material within PBF-LB/M, so there is room for optimizing the process parameters by conventional means [13–15]. Optimization lies primarily in increasing productivity and process robustness. The most straightforward productivity increase can be achieved by adjusting the layer thickness with increased energy input. Productivity is essential for end users in order to increase cost-competitiveness of the process. However, the increase in layer thickness or the number of lasers will increase the formation of process by-products i.e. spatters, which has an extensive influence on the process stability, the laser-powder interaction [16].

This paper studies the effect of He and H_2 additions to the standard Ar process gas for alloy 718 manufactured using PBF-LB/M. Four different gases namely Ar, Ar +30%He, Ar +30%He +2%H_2, and Ar +70%He were used. Previous research has shown He and H_2 addition to reduce spatter generation. In this work, the main focus is to study the effect of these additions on porosity, microstructure and tensile properties for alloy 718. The findings indicate that He and H_2 addition reduces the amount of spatter by 51 % to 89 %. There were no significant differences in the microstructure from the EBSD analysis and the tensile properties were similar. The yield strength and ultimate tensile strength were 1180 MPa and 1395 MPa, respectively. Although the ductility increased from 16.5 % to 17.2 % when processed with pure Ar and Ar + 70%He, respectively. The study shows that there were no significant differences observed, however such processing gases with He and H_2 additions can be increasingly used for higher productivity or novel alloys as it leads to a much more stable process.

2. Material and methods

2.1. PBF-LB/M process

The trials were performed on an EOS M290 (Electro Optical Systems GmbH, Germany) with off-axis optical tomography process monitoring. The schematic of the PBF-LB/M system can be seen in Fig. 1.

Within the PBF-LB/M process, the chamber has to be inertized by the process gas. It limits oxidation of the powder, the melt pool, as well as assures the removal of process by-products. Hence, to compare several gases and isolate their specific properties, the process conditions must be kept equal. This study employed high-quality technical gases such as Ar, He, and their mixtures, also with addition of H_2. Table 1 lists the process gases and an excerpt of their physical properties.

The standard process conditions using argon are set to a differential pressure of 0.56 mbar, equal to a laminar flow of 1.5–2 l/min [17,18].

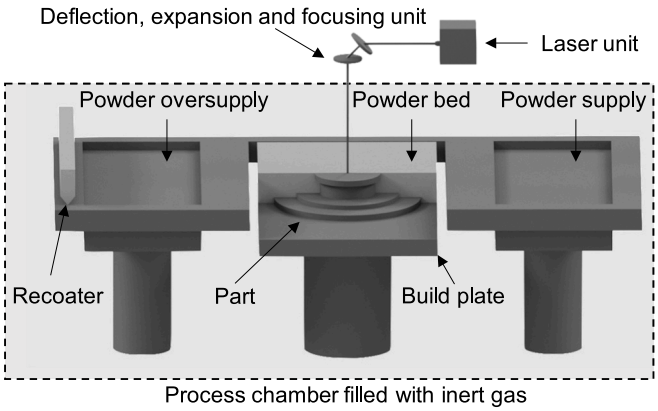

Fig. 1. Core components of a PBF-LB/M machine.

Table 1
Physical properties of used gas mixtures at $p = 1.013$ bar, $T = 0$ °C.

Name	Density ρ in kg/m^3	Thermal conductivity λ in W/(m*K)	Specific heat capacity c_p in J(kg*K)
Ar	1.78	0.02	0.52
He	0.18	0.15	5.19
Ar + 30%He	1.30	0.04	0.71
Ar + 70%He	0.66	0.08	1.41
Ar + 30%He +2%H_2	1.27	0.04	0.74

The flow rate was analyzed before the trials using a Testo 416 vane anemometer to ensure gas comparability. A custom setting was applied for the velocity measurements, followed by a Matlab-based analysis. The experimental velocity setup is presented in Fig. 2. The build plate was partitioned into nine locations where velocities were measured using various differential pressures of 0.1 mbar (EOS machine minimum) to 1 mbar. For all tested gases whose He content was below 70 %, adjusting the differential pressure and, thus, the confining velocity was unnecessary. Using Ar with 70%He, the differential pressure had to be changed.

An off-axis monitoring solution provided by EOS was employed to assess process stability. The EOSTATE Exposure Optical Tomography (OT) monitoring tool uses an sCMOS-based camera. The camera collects light emission per layer in the near-infrared spectrum (900 nm ± 12.5 nm). The dynamic data can provide detailed information about process stability and quality by highlighting indications of insufficient fusion or pronounced heat accumulations. Hence, the maximum data of each layer was exported. Data evaluation and post-processing were conducted using developed scripts based on the freeware ImageJ and Gimp [19]. Through this post-process analysis, process stability by means of the melt pool, by-product amount, and intensity could be investigated. Since the effect on process by-products was favored, the parts were colored white in the OT analysis. Stacking the layer data, interaction zones, and different temperature profiles of process by-products can be made visible.

For each experiment virgin gas-atomized alloy 718 powder with a particle size distribution ranging from 20 µm to 44 µm was used. The powder was provided by Praxair Surface Technologies (PST). The main elemental content is listed in Table 2. All experiments were conducted with the same 40 µm EOS standard parameter (IN718_PerformanceM291 2.11) for alloy 718. Prior to each printing, the process chamber underwent a three-step flushing and purging procedure. To ensure a complete exchange of the atmosphere, purging was stopped at a consistent concentration of 1000 ppm of oxygen, followed by the

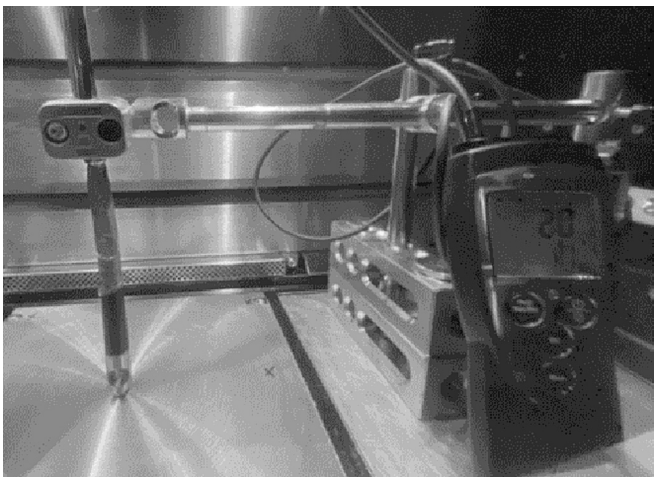

Fig. 2. Setup to measure the gas flow speed on the build plate.

Table 2
Alloy 718 main composition in wt%.

Element	Ni	Cr	Fe	Nb	Mo	Ti	Al	Co
Measured	Bal.	19.27	17.73	4.99	2.94	1.00	0.48	0.33

opening and subsequent closing of the process chamber. This is monitored on the machine system and by the ADDvance 02 precision. The ADDvance 02 precision, developed by Linde, utilizes a chemical cell to accurately analyze oxygen levels, even in the presence of hydrogen-containing gases. The print job was started when reaching process conditions utilizing an oxygen value below 1000 ppm.

The job layout was provided by Siemens Energy and consists of different test specimens to analyze the print quality using tensile properties and microstructure. After printing, all samples were cut using a Klaeger bandsaw bitron 300 without prior stress-relieving heat treatment. After the part removal, the specimen underwent a heat treatment following AMS 5662 [20]. For the chemical analysis of the powder and of the process by-products, a LECO ONH 836 (LECO, US) was used. Before the measurement, three blanks and three standards for nickel-containing material were performed. The mixture of powder and by-products was sampled inside and at the top of the gas outlets of the build chamber.

2.2. Microstructural characterization

For every processing gas, sample cross-sections parallel and perpendicular to the build direction were used for metallographic investigation. The samples were mounted in conductive bakelite resin and ground using SiC papers (#220, #320, #500, #800, #1200) followed by successive diamond suspension polishing (3 µm and 1 µm). The final step of polishing was done using colloidal silica. The cross-section parallel to the build direction was used for porosity measurements using the light optical microscope Zeiss Axioscope 7 with a motorized stage (Zeiss GmbH, Germany). Stitched micrographs at 50× magnification were acquired to obtain the samples' total areal porosity and analyzed using a threshold value-based pore count method using the software ImageJ. To elucidate the changes in porosity in the bulk and subsurface, five micrographs at 100× magnifications were captured in the center and edge of the samples to calculate the bulk and sub-surface porosity, respectively. Then the porosity was measured using the same method as total areal porosity in ImageJ. Electron Backscatter Diffraction (EBSD) was performed using Leo Gemini 1550 SEM equipped with a Nordlys II detector (Oxford Instruments, England). The EBSD acquisition was done on cross-sections parallel and perpendicular to the building direction at an accelerating voltage of 20 kV using a 60 µm aperture and with a step size of 3 µm over an acquisition area of 800 µm × 800 µm. Data clean-up was done using Aztec Crystal software, removing wild spikes and performing noise reduction (seven nearest neighbors required). The EBSD analysis was performed using the open-source MATLAB toolbox MTEX (version 5.9.0) [21]. The indexed EBSD data were used to reconstruct the grain structure and smoothen the grain boundaries, as described in [22]. The grain boundaries considered are high-angle grain boundaries (HAGB) with misorientation >10 degrees. The EBSD orientation maps in inverse pole figure representation were plotted with respect to the build direction. The pole figures were calculated from orientation distribution functions (ODF) which in turn were obtained from the EBSD data. In all the pole figures plotted, the build direction is in the center of the pole figure.

2.3. Tensile testing

All test bars are machined and drawn according to [23,24]. Five tensile specimens were investigated at 20 °C. Subsequently, the results of yield strength (Rp0.2), ultimate tensile strength (Rm), and elongation at fracture (A5) are compared. A Z200 tensile testing machine from Zwick is used to perform the the tensile tests. The traverse speed starts at 0.0007 1/s up to the E-modulus, switches to 0.003 1/s up to Rm, and remains constant at 0.007 1/s.

3. Results and discussion

3.1. Chemical analysis

A visual comparison of the process by-products (also known as spatters) sampled from the gas outlet is depicted in Fig. 3. Fig. 4 exhibits the results of the chemical analysis of the powder-by-product mixture, which was captured inside and on top of the gas outlet. It revealed an increase in oxygen content after printing compared to the virgin powder. The oxygen pickup occurs due to the residual oxygen in the build chamber. This residual oxygen enters the melt pool due to increased absorption affinity and the process-by-products that are emitted from the melt pool have higher oxygen content.

The results show that oxygen pickup was limited by using He or H_2-containing mixtures. The minimal oxygen increase was detected when employing high He fractions in Ar (Ar +70%He), resulting in 331 ± 7 ppm. The maximum oxygen increase of 630 ± 20 ppm has been detected using pure Ar. This might be due to the thermal conductivity and thermal capacity of He and H_2. Hence, they can decrease the intensity and the correlated temperature of process by-products and increase the cooling rate, hence limiting time for oxidation. Pauzon et al. and Deckers et al. indicated similar results using Ti-6Al-4 V and alloy 718 in previous studies [9,19].

A minor difference was observed in analyzing the nitrogen amount. No significant rise in H_2 content was detected, via the carrier gas hot extraction method after each printing process, when material samples were exposed to atmospheres enriched with, He or H_2 during printing.

3.2. Optical tomography

The results of the process by-product analysis are shown in Fig. 5. The process atmosphere has a significant effect on the PBF-LB/M process. The blue area around the parts represents the intensity of process by-products (spatters). Moreover, the intensity and the correlating temperature of process by-products could be significantly reduced using He and H_2-containing mixtures, corresponding to lighter shades of blue around the parts. If the intensity is high, particles can be redeposited and sintered on the surrounding region. This can possibly create a geometrical and/or chemical defect on the next layer. In a comparison of Ar (Fig. 5a) towards the other process gases, a reduction of the "affected" colored area can be seen. Subsequently, adding He or H_2 fractions in argon decreases generation of process by-products. The mixture of Ar +30 %He decreased the total amount of the detected by-products by 40 % and reduced the high critical intensity by 59 % compared to Ar. The highest tested He concentrations of 70 % led to a decrease in the overall generation of by-products by 51 % and 89 % less high-intensity spatter compared to Ar.

As previously reported by Deckers et al. [4], lowering the intensity can reduce surface roughness. Additionally, by reducing the process by-products and laser interaction, bulk density increases due to increased energy coupling [25]. Furthermore, reducing the intensity and amount of redeposited spatter dramatically improves the quality of the recycled powder feedstock [26]. The deleterious effect of process by-products on the part, powder quality, and print stability is already well-known in research [25]. Further investigations are necessary to make a statement regarding an altered cooling behavior. Those could involve simulations and be confirmed by employing melt pool monitoring and penetration depth analysis.

3.3. Porosity analysis

The total bulk porosity of the samples was calculated from cross-

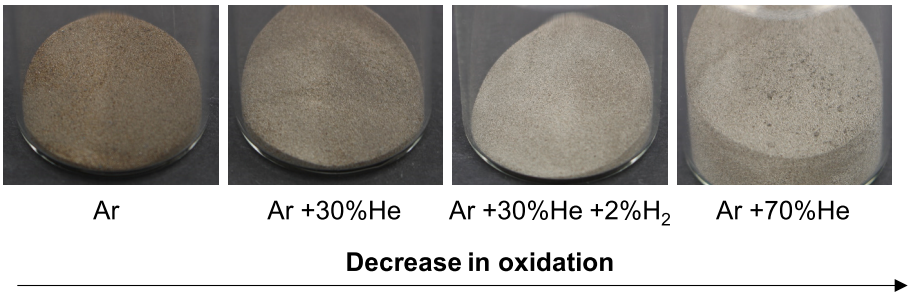

Fig. 3. Visual comparison of process by-products.

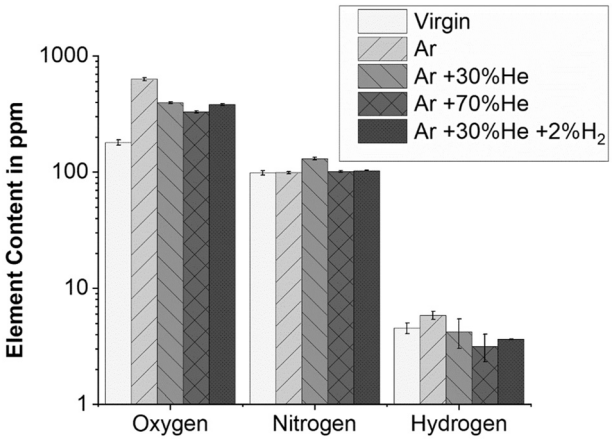

Fig. 4. Elemental analysis of process by-products in ppm.

sections parallel and perpendicular to the build direction for five samples for each process gas as explained in Section 2.2. The results can be found in Fig. 6(a). The pores found were spherical gas pores and a representative micrograph of microstructure processed with Ar is shown in Fig. 6(b). The Ar samples had the highest porosity of 0.08 % on average and the highest standard deviation of 0.04 %. Adding H_2 or He to the process gas resulted in a reduction in porosity. The lowest porosity of 0.04 % with a standard deviation of 0.02 % was detected under an Ar +70%He atmosphere. The maximum defect size in the bulk material ranges from 11.98 to 15.18 µm.

However, comparing bulk and sub-surface porosity revealed that the sub-surface porosity was marginally higher than the bulk porosity. Within the subsurface analysis, the maximum defect size varies between 31.80 and 55.14 µm. Although the focus of this study was not to find optimized surface porosity, the results should not affect tensile performance due to the machined surface of the tensile specimen. The subsurface analysis also indicates a porosity reduction using He and H_2-containing process gases.

Previous studies on different alloys have shown a slight reduction in porosity by adding He to the processing gas which is similar to this study [4,6,10]. Traoré et al. [7] highlighted that PBF-LB/M processed alloy 625 possessed porosity that was slightly lower or similar for He processed samples compared with Ar for a wide range of volumetric energy densities (48–72 J/mm^3). However, at high volumetric energy densities, the porosity for the He processed sample was <0.05 %, while the Ar samples had a porosity of 0.12 %. This finding agrees with Deckers et al. [19] and Pauzon et al. [6] where it was showed that samples processed under Ar gas mixtures with He addition and pure He consistently had lower porosity values than sample processed under Ar gas. The reduction in porosity is attributed to the improved process stability and reduced process-by-products (spatter) generation, obtained when using the gas mixtures with He addition. The reduction in spatter results is

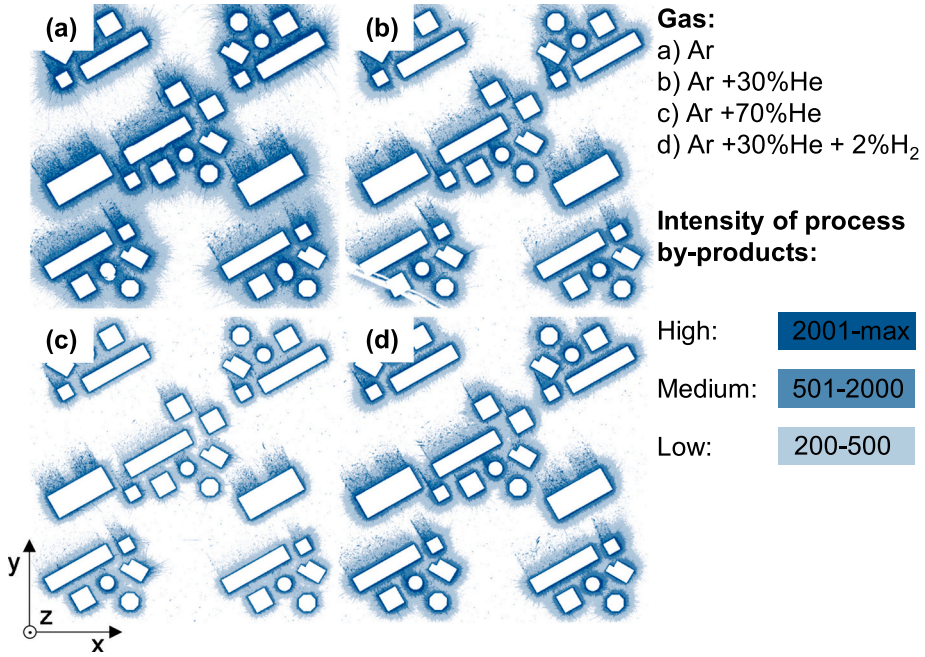

Fig. 5. OT analysis of the investigated gas mixtures highlighting the amount and intensity of process by-products.

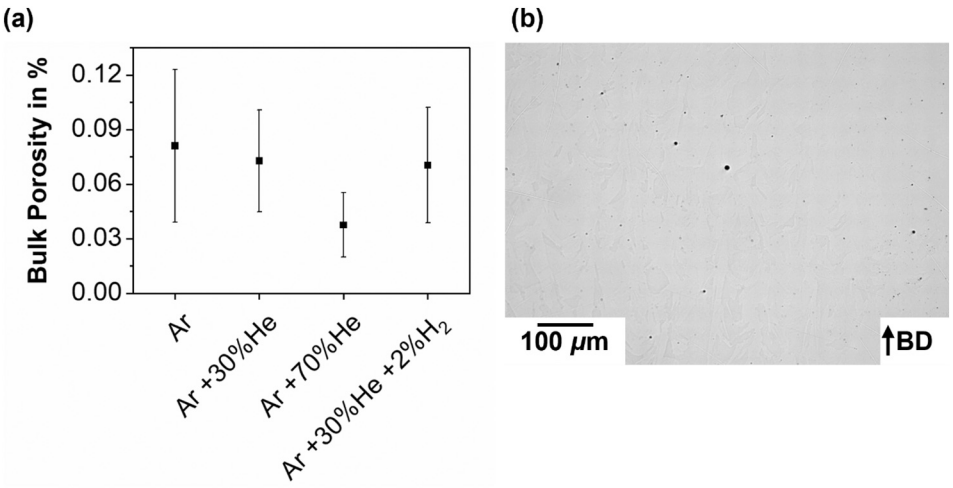

Fig. 6. (a) Bulk porosity for different gas mixtures, (b) optical micrograph showing the presence of bulk porosity (in a sample processed in Ar).

outcome of the more stable melt pool from one side and lower spatter re-deposition on the printed sample, leading to the bulk porosity reduction [27]. Furthermore, the Ar-He mixture could also affect the melt pool cooling rates and flow [28]. It can be assumed that an improvement in part density can also be achieved irrespective of the alloy, as was already shown in case of Ti-6Al-4V. Therefore, using low-density and high thermal conductivity gases like mixtures of Ar with He or H_2 is particularly advantageous when developing new parameters, e.g., for novel alloys or improving present parameter sets.

3.4. Microstructure

The EBSD orientation maps in inverse pole figure (IPF) coloring are shown in Fig. 7. EBSD acquisitions were performed in cross-sections parallel and perpendicular to the build direction (BD) for the samples processed in four different gas atmospheres. The IPF coloring is with

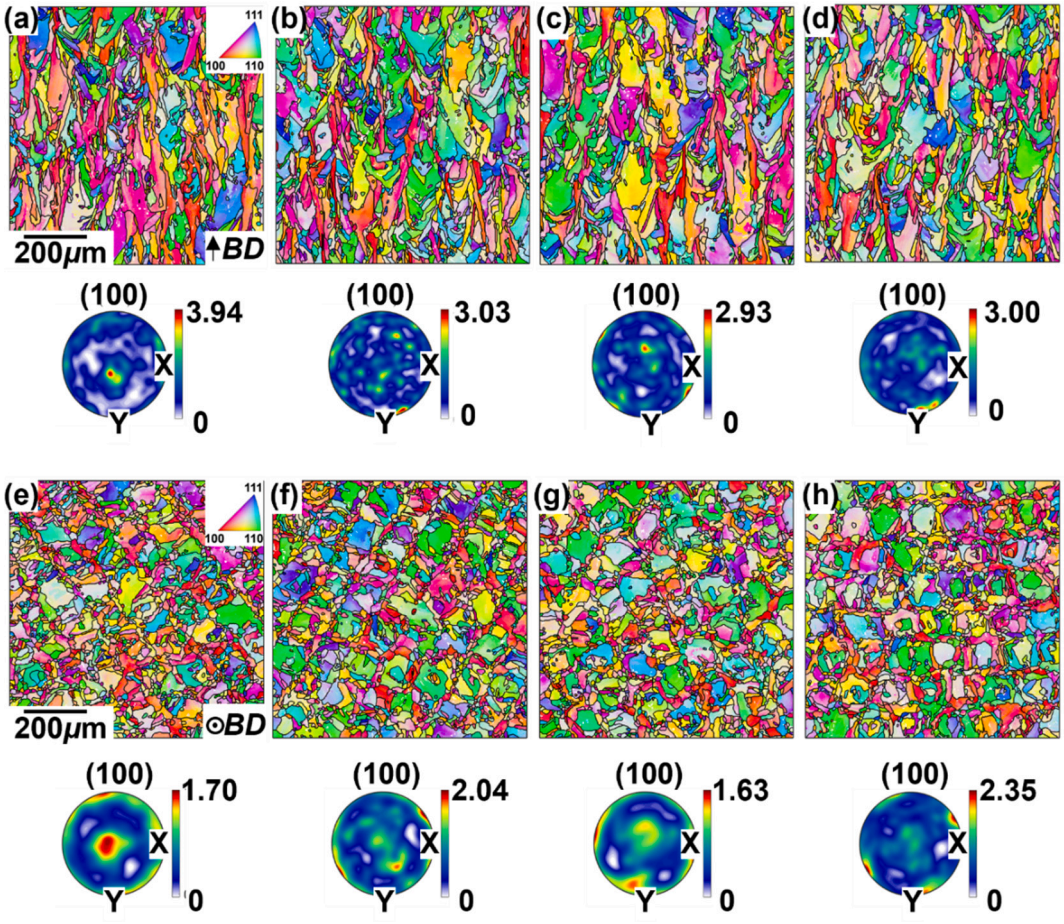

Fig. 7. EBSD orientations maps with IPF coloring along with the pole figures for different process gases (a,e) Ar, (b,f) Ar +30%He, (c,g) Ar +70%He and (d,h) Ar +30%He +2%H_2.

respect to the build direction. In the pole figures, the build direction is in the center. The black arrows in (a) and (e) indicate the melt pool overlap region. A striking similarity in all the samples is the memory of the PBF-LB/M printing, which is evident from the melt pool structures (parallel to the BD) and the scan tracks (perpendicular to the BD) even after heat treatment. The presence of finer grains with ⟨100⟩ orientation (marked in Fig. 7(a), (e) with black arrows) in the melt pool overlapping region is also observed from the orientation maps. Overall, the samples processed in different atmospheres seem similar. The only exception is the Ar processed samples (Fig. 7(a), (e)) which have a relatively higher intensity at <100>, but this is merely because a slightly higher fraction of grains that are oriented in <100> or nearly <100> direction. The grain size estimates from the orientation maps, parallel and perpendicular to the build direction, were similar for the samples processed with different gases. The area-weighted mean grain size was ~100 μm parallel to the build direction and ~40 μm perpendicular to the build direction. The estimates were based on the fitted ellipse primary length and equivalent circle diameter for the sample parallel and perpendicular to the build direction, respectively. This is due to the nature of the columnar grains parallel to the build direction and equiaxed-like perpendicular to the build direction.

Hence, helium or hydrogen-containing gases influence grain morphology has yet to be clarified. Amano et al. [10] highlighted a microstructure refinement when Ti-6Al-4 V samples were processed using He. A finer presence of martensitic α′ was found in He samples which was caused due to the higher cooling rates. This is in contrary to the findings of Pauzon et al. [9]. Another study by Traoré et al. [7] reported also no change on alloy 625 microstructure when processed under Ar and He. Pauzon et al. [29] reported the presence of a random texture for alloy 718 processed under Ar and Ar-He mixture. Within this study, the microstructure was not affected by the different processing gases studied, which was also observed by Traoré et al. [7] and Pauzon et al. [29]. It is, however, possible that there are differences in the sub-microstructure when processing with the different processing atmospheres, that were not detected at the applied magnification of EBSD and were not observed by the authors in previous works during more detailed analysis of the microstructure on the micro-scale in case of Ar-He-containing atmospheres [30]. Based on the available literature, it also seems that the differences are material- and process-specific, as impact of processing gas on microstructure was observed in the Ti-6Al-4 V microstructure by Amano et al. [10]. Hence, it can be said that although there could be differences in cooling rates, there were no changes in the microstructure with the different processing atmospheres for Alloy 718.

3.5. Tensile properties

The results of the tensile properties along the build direction can be found in Fig. 8. The tensile values for alloy 718 from the data sheet (DS) by technology provider EOS were taken as a reference [31]. The achieved tensile performance for 20 °C is comparable to the literature [32]. The tensile properties were not significantly affected by the processing gas. The yield and ultimate tensile strength for different samples were approximately 1180 MPa and 1395 MPa, respectively. However, there was a slight increase in ductility from 16.5 % to 17.2 %, when processed with pure Ar and Ar + 70%He. The addition of H2 appears to cause some loss in ductility. A fracture surface analysis revealed no noticeable difference between the tested samples that could explain this effect. Potential differences might be due to the heat treatment or the time between sample testings. The slight increase in properties were also reported by Pauzon et al. for Ti-6Al-4V [6]. This beneficial increase in properties can be attributed to the improved stability of the process, hence reduction in spatter formation and resulting porosity as the microstructure was not found to be affected by the processing atmosphere. This minimal difference observed with different processing gas can be highly beneficial in industrial applications when printing larger components, especially when using higher layer thickness. There is also clear impact on sustainability and cost effectiveness of the process through improvement of the powder reuse as a result of lower spatter formation and hence decreased powder degradation in case of He-containing atmospheres.

4. Conclusion

This study analyzed the influence of the different process atmospheres on alloy 718 manufactured by PBF-LB/M. The four gases studied were Ar, Ar +30%He, Ar +30%He +2%H_2, and Ar +70%He. The findings indicate that the spatter generation was reduced by He addition to the standard Ar gas. This is attributed to the higher thermal conductivity of He and hence He-containing processing gases, resulting in faster spatter cooling and hence lower oxidation of the spatter. This was confirmed by lower oxygen pickup by spatter particles (around 300 ppm) when processed using He and H_2 containing process atmospheres when compared to Ar. The decrease in porosity by 0.04 % for Ar + 70% He when compared with Ar can be attributed to the reduction in spatter which probably led to improved process stability. The microstructure was not affected by the different processing gases and the EBSD revealed that there is a random texture with similar grain sizes (~100 μm parallel to the build direction and ~40 μm perpendicular to the build direction). There was also the presence of melt pools and scan tracks from the PBF-LB/M process. Similar tensile properties were obtained for the samples with different processing atmospheres. The yield and ultimate tensile strength were approximately 1180 MPa and 1395 MPa, respectively. However, there was a slight increase in ductility from 16.5 % to 17.2 %, when processed with pure Ar and Ar + 70%He, respectively. Tensile properties for sample processed under Ar +30%He +2%H_2 were similar except for the decrease in ductility by 1 % when compared with sample processed under Ar +30%He. A stable process with reduced spatter and porosity with increasing He addition is attributed to the beneficial increase in ductility.

This study shows the importance of the processing gas during the PBF-LB/M process. Utilizing Ar with He additions have proven to lead to a more stable process with reduction in spatters and porosity. This has found to have a benefit in the tensile properties where the yield strength,

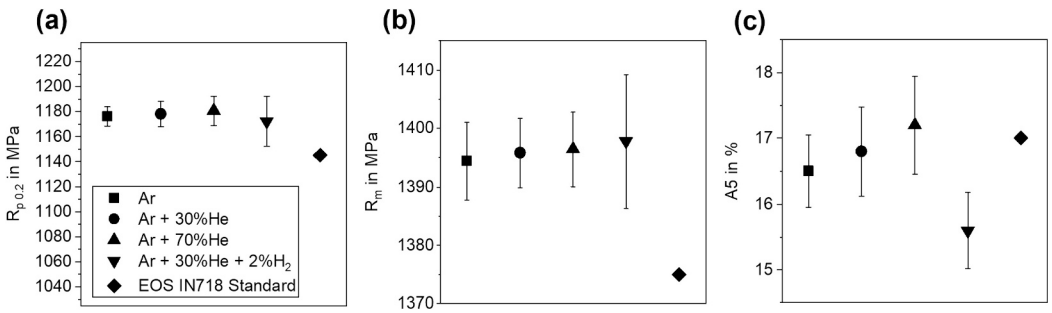

Fig. 8. Results of tensile specimen analyzed at 20 °C (a-c). $Rp_{0.2}$ is the 0.2 % offset yield strength. Rm is the ultimate tensile strength. A5 is the elongation.

ultimate tensile strength and ductility were increased with increased He addition to the standard Ar process gas used in the PBF-LB/M process.

CRediT authorship contribution statement

T. Deckers: Writing – review & editing, Writing – original draft, Visualization, Validation, Supervision, Software, Resources, Project administration, Methodology, Investigation, Formal analysis, Data curation, Conceptualization. **A. Fardan:** Writing – review & editing, Writing – original draft, Visualization, Validation, Methodology, Investigation, Formal analysis, Conceptualization. **L. Kersting:** Writing – original draft, Investigation. **A. Kreutzer:** Resources. **P. Forêt:** Writing – review & editing, Supervision, Resources, Project administration. **S. Dubiez-Le Goff:** Writing – review & editing, Writing – original draft, Supervision. **G. Witt:** Writing – review & editing. **S. Kleszczynski:** Writing – review & editing. **U. Klement:** Writing – review & editing, Writing – original draft, Supervision. **E. Hryha:** Writing – review & editing, Writing – original draft, Supervision.

Declaration of competing interest

The authors declare that they have no known competing financial interests or personal relationships that could have appeared to influence the work reported in this paper.

Data availability

The data supporting this study's findings are available from the corresponding author T. Deckers upon reasonable request.

Acknowledgments

A. Fardan and E. Hryha would like to acknowledge the Centre for Additive Manufacturing - Metal (CAM^2) supported by the Swedish Governmental Agency for Innovation Systems (Vinnova). A. Fardan would like to acknowledge Håkan Brodin (Siemens Energy, Finspång, Sweden) for discussion about tensile properties.

Siemens Energy would like to acknowledge the financial support by the European Regional Development Fund (ERDF) via "ProFIT HTA High-Temperature Applications" No. 10167478.

References

[1] Wohlers TT, Campbell I, Diegel O, Huff R, Kowen J. Wohlers report 2022: 3D printing and additive manufacturing global state of the industry. Fort Collins, Colorado: Wohlers Associates; 2022.
[2] DIN EN ISO/ASTM 52900:2022-03, Additive Fertigung_- Grundlagen_- Terminologie (ISO/ASTM 52900:2021); Deutsche Fassung EN_ISO/ASTM 52900: 2021, Berlin, Beuth Verlag GmbH.
[3] Volpato GM, Tetzlaff U, Fredel MC. A comprehensive literature review on laser powder bed fusion of Inconel superalloys. In: Additive manufacturing; 2022.
[4] Deckers T, Ammann T, Forêt P, Dubiez-Le-Goff S, Zissel K, Witt G. Einfluss heliumhaltiger Prozessgase auf den Laser-Strahlschmelzprozess. In: Zeitschrift für wirtschaftlichen Fabrikbetrieb; 2022.
[5] Bidare P, Bitharas I, Ward RM, Attallah MM, Moore AJ. Laser powder bed fusion in high-pressure atmospheres. In: The International Journal of Advanced Manufacturing Technology; 2018.
[6] Pauzon C, Forêt P, Hryha E, Arunprasad T, Nyborg L. Argon-helium mixtures as laser-powder bed fusion atmospheres: towards increased build rate of Ti-6Al-4V. In: Journal of Materials Processing Technology; 2020.
[7] Traoré S, Koutiri I, Schneider M, Lefebvre P, Rodrigues J, Dupuy C, et al. Influence of gaseous environment on the properties of Inconel 625 L-PBF parts. In: Journal of Manufacturing Processes; 2022.
[8] VDI e. V: VDI-Wärmeatlas, Berlin, Heidelberg, Springer Berlin Heidelberg, 2013.
[9] Pauzon, C.; van Petegem, S.; Hryha, E.; Sin Ting Chang, C.; Hocine, S.; van Swygenhoven, H.; Formanoir, C. de; Dubiez-Le Goff, S.: Effect of helium as process gas on laser powder bed fusion of Ti-6Al-4V studied with operando diffraction and radiography, In: European Journal of Materials, 2022.
[10] Amano, H.; Ishimoto, T.; Suganuma, R.; Aiba, K.; Sun, S.-H.; Ozasa, R.; Nakano, T.: Effect of a helium gas atmosphere on the mechanical properties of Ti-6Al-4V alloy built with laser powder bed fusion: a comparative study with argon gas, In: Additive manufacturing, 2021.
[11] Schafrik, R. E.; Ward, D. D.; Groh, J. R.: Application of alloy 718 in GE aircraft engines: past, present and next five years, in: Superalloys 718, 625, 706 and various derivatives (2001), TMS, 2001.
[12] Benini E. Advances in gas turbine technology. Benini, Ernesto (Hrsg.). Rijeka, Croatia: Intech; 2011.
[13] Marques A, Cunha Â, Silva MR, Osendi MI, Silva FS, Carvalho Ó, et al. Inconel 718 produced by laser powder bed fusion: an overview of the influence of processing parameters on microstructural and mechanical properties. In: The International Journal of Advanced Manufacturing Technology; 2022.
[14] Wang X, Gong X, Chou K. Review on powder-bed laser additive manufacturing of Inconel 718 parts. In: Proceedings of the Institution of Mechanical Engineers, Part B: Journal of Engineering Manufacture; 2017.
[15] Rott S. Homogenisierung lokaler Prozesscharakteristika für das Laserstrahlschmelzen; 1. Auflage: RWTH Aachen University; 2022.
[16] Taheri Andani M, Dehghani R, Karamooz-Ravari MR, Mirzaeifar R, Ni J. Spatter formation in selective laser melting process using multi-laser technology. In: Materials & design; 2017.
[17] Ladewig A, Schlick G, Fisser M, Schulze V, Glatzel U. Influence of the shielding gas flow on the removal of process by-products in the selective laser melting process. In: Additive manufacturing; 2016.
[18] Reijonen J, Revuelta A, Riipinen T, Ruusuvuori K, Puukko P. On the effect of shielding gas flow on porosity and melt pool geometry in laser powder bed fusion additive manufacturing. In: Additive manufacturing; 2020.
[19] Deckers T, Ammann T, Forêt P, Witt G. An optical tomography based study on the influence of different gases during PBF-LB/M: distribution of process by-products and part properties. In: Proceedings of the 18th Rapid.Tech 3D Conference Erfurt, Germany, 17–19 June 2022; 2022. München.
[20] SAE AMS 5662P:2022-08-17 Rings, 52.5Ni - 19Cr - 3.0Mo - 5.1Cb (Nb) - 0.90Ti - 0.50AI - 18Fe, Consumable Electrode or Vacuum Induction Melted, 1775 °F (968 °C) Solution Heat Treated, Precipitation-Hardenable, 400 Commonwealth Drive, Warrendale, PA, United States, SAE International.
[21] Bachmann F, Hielscher R, Schaeben H. Texture analysis with MTEX – free and open source software toolbox. In: Solid state phenomena; 2010.
[22] MTEX: Fill Missing Data in Orientation Maps, https://mtex-toolbox.github.io/EBSDFilling.html (abgerufen am: 21.06.2023).
[23] DIN EN ISO 6892-1:2020–06, Metallische Werkstoffe_- Zugversuch_- Teil_1: Prüfverfahren bei Raumtemperatur (ISO_6892–1:2019); Deutsche Fassung EN_ISO_6892–1:2019, Berlin, Beuth Verlag GmbH.
[24] DIN EN ISO 6892-2:2018–09, Metallische Werkstoffe_- Zugversuch_- Teil_2: Prüfverfahren bei erhöhter Temperatur (ISO_6892–2:2018); Deutsche Fassung EN_ISO_6892–2:2018, Berlin, Beuth Verlag GmbH.
[25] Li Z, Li H, Yin J, Li Y, Nie Z, Li X, et al. A review of spatter in laser powder bed fusion additive manufacturing: in situ detection, generation, effects, and countermeasures. In: Micromachines; 2022.
[26] Gasper A, Szost B, Wang X, Johns D, Sharma S, Clare AT, et al. Spatter and oxide formation in laser powder bed fusion of Inconel 718. In: Additive manufacturing; 2018.
[27] Schwerz C, Raza A, Lei X, Nyborg L, Hryha E, Wirdelius H. In-situ detection of redeposited spatter and its influence on the formation of internal flaws in laser powder bed fusion. In: Additive manufacturing; 2021.
[28] EPMA (Hrsg.); Deckers, T. (Mitarb.): World PM 2022 Congress Proceedings: A Study on the Influence of Different Process Gases on Selectively Laser Melted Nickel-Chromium Powder by Means of Process Monitoring: Melt Pool Geometries and Process By-Product Characteristics, 2022.
[29] Pauzon C, Mishurova T, Fischer M, Ahlström J, Fritsch T, Bruno G, et al. Impact of contour scanning and helium-rich process gas on performances of Alloy 718 lattices produced by laser powder bed fusion. In: Materials & design; 2022.
[30] Pauzon C, Markström A, Dubiez-Le Goff S, Hryha E. Effect of the process atmosphere composition on alloy 718 produced by laser powder bed fusion. In: Metals; 2021.
[31] EOS GmbH: EOS NickelAlloy IN718: Material Data Sheet, https://www.eos.info/03_system-related-assets/material-related-contents/metal-materials-and-examples/metal-material-datasheet/nickelalloy-inconel/material_datasheet_eos_nickelalloy_in718_01-23_en.pdf (abgerufen am: 22.06.2023).
[32] Morgan, K.; Wells, D.: Overview of Fatigue and Damage Tolerance Performance of SLM Alloy 718, National Space and Missile Materials Symposium, https://ntrs.nasa.gov/api/citations/20160007853/downloads/20160007853.pdf.